Numerical study of dense powder flow in a rotating drum: Comparison of CFD to experimental measurements

Lucas Chatre, Xavier Lemerle, Marc Bataille, Florian Herbelet, Marie Debacq, Jeremy Nos, Khashayar Saleh, Mikel Leturia, Tojonirina Randriamanantena

Numerical study of dense powder flow in a rotating drum: comparison of CFD to experimental measurements

Lucas Chatre[a,b], Xavier Lemerle[a], Marc Bataille[a], Florian Herbelet[a], Marie Debacq[b,c], Jeremy Nos[d], Khashayar Saleh[e], Mikel Leturia[e], Tojonirina Randriamanantena[a,*]

a, CEA, DES, ISEC, DMRC, Université de Montpellier, Marcoule,
b, Université Paris-Saclay, INRAE, AgroParisTech, UMR SayFood, 91120, Palaiseau, France
c, CNAM, 2 rue Conté, 75003 Paris, France
d, ORANO Recyclage,125 Avenue de Paris, 92320, Châtillon, France
e, Université de Technologie de Compiègne, ESCOM, TIMR (Integrated Transformations of Renewable Matter), Centre de Recherche Royallieu - CS 60319 - 60 203 Compiègne Cedex, France
* Corresponding author. E-mail address Tojonirina.RANDRIAMANANTENA@cea.fr (T. Randriamanantena).

ABSTRACT

Designing chemical reactor equipment requires a thorough understanding of powder flow. Solid rheology modelling offers various models for this purpose. A comparative study of two different CFD models, the Kinetic Theory of Granular Flow (KTGF) and the dense granular flow ($\mu(I)$ law), is proposed. Both models were confronted with experimental results obtained on a rotating drum for different rotation speeds and powder flowabilities. Image processing was used to compare the experimental gas/solid interfaces with those obtained from CFD. The KTGF model did not represent the powder rheology at low rotation speeds, regardless of the powder, whereas it was closer to experiments at higher speeds. The dense granular flow model was more appropriate for this system as it described the powder shape inside a rotating drum relatively well for each experiment. The latter model is recommended for modelling dense granular flows, while the KTGF is better suited to gas-solid flows.

Keywords: CFD, Dense solids flow, Rotating drum, Image processing, Modelling, $\mu(I)$ law

NOMENCLATURE

α	Phase volume fraction (-)
$\alpha_{s,max}$	Maximum volume fraction that can reach the solid (-)
$\alpha_{s,min}$	Minimum volume fraction below friction is not calculated (-)
c	Cohesion of the powder (Pa)
CI	Cohesive index (-)
C_s	Random fluctuation velocity (m/s)
D	Drum diameter (m)
d_p	Mean particle diameter (m)
D_x	Particle diameter (with x the sample weight percentage having diameter less than D_x) (m)
d_{32}	Sauter diameter (m)
e	Restitution coefficient (-)
η	Effective viscosity (Pa.s)
η_{adh}	Adhesion index (-)

η_{max}	Maximum viscosity (Pa.s)
f_c	Adhesion force (kg.m.s^{-2})
$f_{\sigma i}$	Surface tension (kg.m^{-2}.s^{-2})
g	Gravitational acceleration (m s^{-2})
g_0	Radial distribution (-)
$\dot{\gamma}$	Shear rate (s^{-1})
HR	Hausner ratio (-)
I	Inertial number (-)
I_c	Modified inertial number (-)
I_0	Constant for the $\mu(I)$ law (-)
L	Drum depth (m)
M	Rate of interfacial momentum transfer (kg.m^{-2}.s^{-2})
μ	Friction coefficient (-)
μ_{gs}	Granular shear viscosity (Pa.s)
$\mu_{gs,col}$	Collision viscosity (Pa.s)
$\mu_{gs,kin}$	Kinetic viscosity (Pa.s)
$\mu_{gs,fric}$	Friction viscosity (Pa.s)
μ_2, μ_s	Critical values for the $\mu(I)$ law (-)
MAE	Mean absolute error (m)
N	Rotation speed (min^{-1})
ω	angular rotation speed (rad/s)
P	Normal pressure (Pa)
RMSE	Root mean square error (m)
ρ	Density (kg.m^{-3})
ρ_{bulk}	Bulk density (kg m^{-3})
ρ_s	Solid density (kg.m^{-3})
ρ_{tap}	Tapped density (kg.m^{-3})
S	Momentum source term (kg.m^{-2}.s^{-2})
τ	Shear stress (Pa)
θ_r	Static angle of repose (°)
θ_D	Dynamic angle of repose (°)
Θ_s	Granular temperature (m^2.s^{-2})
U	Velocity (m/s)
y_i	Predicted ordinate (m)
y_i^*	Experimental ordinate (m)

1. INTRODUCTION

It is estimated that 60% of all chemical products sold are at a solid state [1]. Yet, granular flow is not fully understood and is still under thorough study [2,3]. Understanding the solids flow inside chemical reactor equipment is critical to predicting the reactor performance or designing the reactor itself. Yet, powder flowability cannot be assessed with only one indicator [4]. Several parameters have to be measured to estimate powders flowability and rheology (i.e. static angle of repose, Hausner ratio, etc.) [5]. Choosing which characteristics to measure depends on the conditions undergone by the particles within the equipment [5].

As an example, the dynamic angle of repose, which is the slope angle taken by the powder as it flows, can be measured from the rotating drum [6]. The flowability of the powder can be estimated from the dynamic angle of repose: the lower it is, the better the flowability [7]. Some authors proposed other characteristic parameters obtained from the interface, for instance the interface fluctuation over time, to capture more information on the powder flowability [8]. Many chemical reactors involving a solid phase have a flow pattern similar to a rotating drum [9–12]. The rotating drum, in which solid particles flow freely at the surface over a static granular bed, has been extensively studied experimentally [8,13–15]. Due to the simplicity of its geometry, the rotating drum is a frequently used device to understand dense granular flow dynamics. Therefore, the solid motion in this device for different rotation speeds and filling degree is relatively well understood for free flowing powder [7].

Numerical simulations of powder flow in rotating drum is also very common. For solid flow simulations, Discrete Element Method (DEM) and Computational Fluid Dynamic (CFD) are the main methods. The first follows the trajectory of each individual particle while modelling inter-particle and wall particle interactions [16]. Collision-free motion is represented with Newton's second law, while normal and tangential collisions are simulated with Hooke's law (spring force). All the equations used are detailed in the literature [17–19]. Particle flow in a rotating drum has been studied using DEM [20–22]. Discrete element method can provide a very detailed and accurate description of the granular flow for adequate cases, yet it can be time consuming for high number of particles [23].

On the other hand, following an Eulerian approach, CFD simulation assimilates the flow of the powder to that of a fluid as a whole. Flow can then be described by the conservation of mass, momentum and energy using finite volume method. CFD has been used for rotating drum simulation [24–28]. CFD simulations can be a good candidate for dense granular flow of fine particles, as it is not limited by the number of particles simulated.

One of the best-known models to represent the flow of solid particles is the Kinetic Theory of Granular Flow (KTGF) [29]. Such model has been mainly used for fluidised bed [30–33]: the KTGF model is more adapted for the "gaseous" regime where the solid phase is strongly agitated within the air [34]. Yet, the KTGF model has also been used for solid flow simulation in a rotating drum [24,25,27,35]. Another known model is the dense granular flow model, also called the $\mu(I)$ law [2]. This model is more adapted for the "liquid" regime [34]. Such model has been used for sediment transport [36], granular flow on a pile [34] or even the discharge of a granular silo [37]. Arseni et al. [28] used the $\mu(I)$ law to model the solid flow inside a rotating drum with particles having a diameter larger than 1 mm. The model is able to catch the powder bed shape and even the velocity when compared with experimental results. Yet, to our knowledge, the $\mu(I)$ law has not been studied for powder flow (diameter less than 100 µm).

For both simulation approaches, the main concern is to find the adequate model that best represents the solid rheology. In this work, we studied experimentally the powder flow inside a rotating drum. Image processing was performed to extract the gas/solid interface. Two rheological models implemented in the CFD code were compared with the experiments: one using the multiphase flow modelling approach and one using the Volume of Fluid (VOF) approach. The aim of this work is to find which CFD model is the most suitable for powder flow in a rotating drum for a given rotation speed and powder flowability.

2. EXPERIMENTAL SETUP

2.1. Experimental device

The rotating drum used is a commercial apparatus from Granutools named GranuDrum™. More details are given in this paper [8]. Figure 1 shows a scheme of the rotating drum. The drum diameter is D=84 mm with a depth of L=20 mm. The rotation speed of the drum can vary from 1 RPM to 80 RPM. To get the powder bed shape, the drum is placed between a lighting system and a monochrome camera. The image resolution is 406x406 pixels. A software from Granutools is used to control the drum rotation speed, the exposure time of the camera, the total number of images taken during the experiment and the frame rate. For each experiment, at least three drum revolutions were recorded to ensure a steady state.

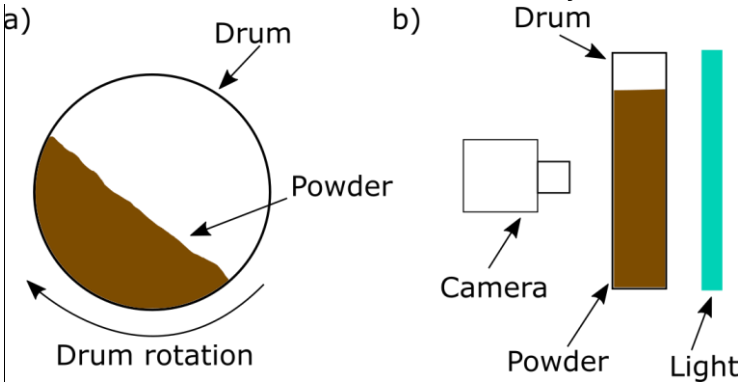

Figure 1: Scheme of the rotating drum a) front view and b) side view

The software provides an image processing algorithm for the interface detection, described in [8]. Powder flowability parameters are calculated from the interface detected, also described by Neveu et al. [8]. Here, we will mainly focus on the dynamic angle of repose noted θ_D and on the cohesive index noted CI. The former is the angle taken by the slope during the rotation, calculated at the drum centre, within a window of D/5. The dynamic angle of repose characterises the powder flowability: the higher it is, the poorer the flowability. Knowing this parameter helps to understand powder flow in dense flow apparatus [6]. The cohesive index characterises the interface fluctuation during the rotation, according to equation 1.

$$CI = \frac{1}{D_{crop}} \cdot \sum_{x} \sqrt{\frac{\sum_{i=1}^{N_y(x)} \left(\bar{y}(x) - y_i(x)\right)^2}{N_y(x)}} \quad (1)$$

With D_{crop} the cropped diameter (discussed in section 2.3.1), $N_y(x)$ the number of interface pixel ordinates, $\bar{y}(x)$ the average interface ordinate for an abscissa x and $y_i(x)$ the interface ordinate for an abscissa x, the sum is performed on the whole set of abscissa belonging to the cropping zone [8]. A high cohesive index means a high fluctuation of the interface, which is characteristic of cohesive powders [8].

2.2. Powder used and their flowability properties.

The powder bed shape in a rotating drum was studied with three different powders. Powder flowability properties are listed in Table 1. The d_{32} diameter, also called the Sauter diameter, is calculated according to equation 2, where n is the total number of particles and n_i is the number of particles of diameter d_i. [38]

$$d_{32} = \frac{\sum_i^n n_i . d_i^3}{\sum_i^n n_i . d_i^2} \quad (2)$$

More information on the device used to characterise the powder flowability is given in a previous study [10]. From this previous study, it has been concluded that the Hausner ratio, noted HR ($HR = \rho_{tap}/\rho_{bulk}$), is a more precise measurement method compared to the static angle of repose, noted θ_r, to estimate powder flowability. The Hausner ratio compares the tapped density over the bulk density. Having a lower static angle of repose and/or a lower Hausner ratio means that the powder is more flowable. According to Leturia et al. [4], brown corundum F180 and glass powder are considered to be non-cohesive powders (free flowing) with a Hausner ratio lower than 1.30 while the rice flour is considered as cohesive with a Hausner ratio higher than 1.40. The Geldart classification is obtained from [39] using the particle density and the mean diameter. The ρ_s is calculated from ρ_{bulk}, assuming an overall solid volume fraction of 0.60 [40]

Table 1: Flowability properties of studied powder

	ρ_{bulk} (kg m^{-3})	ρ_s (kg m^{-3})	θ_r (°)	HR (-)	D10 (µm)	D50 (µm)	D90 (µm)	d_{32} (µm)	Geldart classification
Brown corundum F180	1815	3025	31	1.17	50	81	125	66.5	A
Glass powder	924	1540	38	1.27	53	114	191	61.6	A
Rice flour	549	915	43	1.42	24	96	165	39.2	A

2.3. Detection of the interface

2.3.1. Image processing for the experimental interface detection

The GranuDrum™ software does not give the gas/solid interface coordinates. Therefore, image processing was performed to obtain the experimental interface coordinates. Images recorded by the camera were analysed using a Python script (available https://gitlab.com/lchatre/imageanalysispowder/).

First, a circular cropping region is defined so as not to be disturbed by any powder adhering to the wall (Figure 2). It can be seen that some fine particles adhere to the wall for relatively flowable powder (Figure 2a, centre right) while block of powders are completely stuck at the drum wall for less flowable powder (Figure 2b, opposite to the powder flow). Thus, the cropped region was defined as 20% for brown corundum F180 and glass powder experiments (Figure 2a); 40% for rice flour experiments (Figure 2b), meaning that 80% of drum is considered for the brown corundum F180 and glass powder, while 60% is considered for rice flour. The crop percentage (noted per_{crop}) corresponds to the total surface (*i.e.* drum diameter D) of the rotating drum (powder and air) not taken into account for image processing. Consequently, the cropped diameter D_{crop} of the circle considered for image processing (after cropping) can be calculated as $D_{crop} = \left(1 - per_{crop}\right)D$.

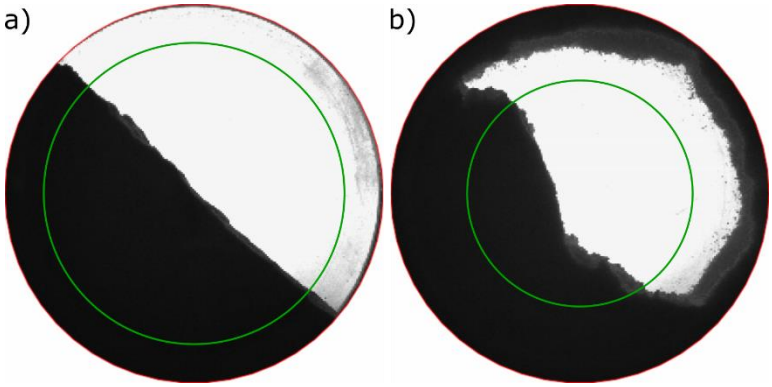

Figure 2: Powder adhering to the wall during the experiment for a) non-cohesive powder (HR=1.27) and b) cohesive powder (HR=1.42). The cropping zone is in green.

The HSV colour space, recommended by Bora *et al.* [41] for colour image segmentation, was used for image processing. The HSV values of the studied powder and the gas atmosphere are obtained at the initial frame (Figure 3a). Then, the image processing is performed on every image taken during the drum rotation (Figure 3b).

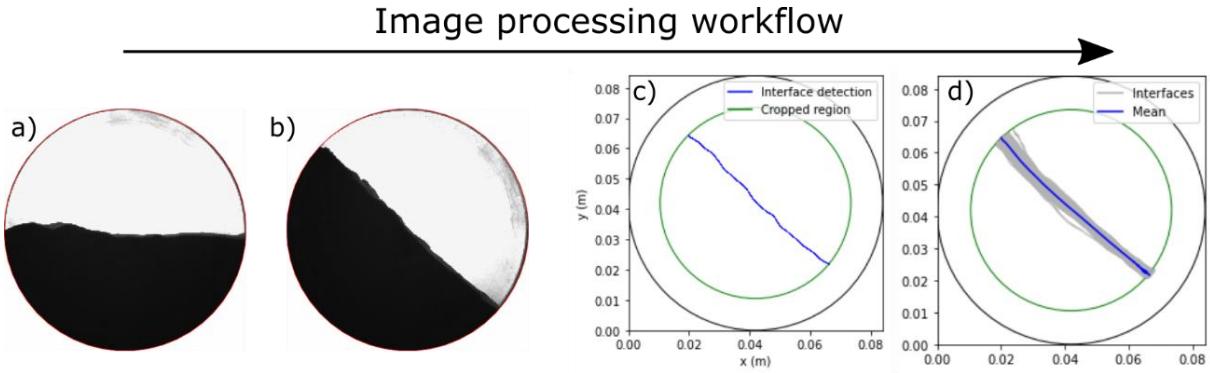

Figure 3: Image processing for the interface detection: a) initial frame, b) powder bed shape during the experiment, c) extraction of the interface coordinates and d) all interfaces averaged. The interfaces in grey are the experimental interface fluctuations.

A mask is used to extract pixel belonging to the HSV value of the studied powder and those that belong to the HSV value of the gas atmosphere. Both masks are then extended and pixels where both masks are present are identified as the interface. This method shows similar results when compared with a Sobel operator. Those interface pixels are then converted into coordinates (Figure 3c and Figure 3d).

The variation of the average interface with the number of images used is plotted on Figure 4. It can be seen that the average interface is similar for more than 30 images analysed. In order to have more information on the interface fluctuation, 90 images were analysed and all the interface coordinates were averaged (Figure 3d) for every experiment. Moreover, recording at least more than three times the required time for a stable average interface (obtained for 30 images) allows having reliable time-averaged results on the average interface. The grey curves represent all the interfaces taken during the experiment while the blue one represents the average. Neveu et al. [8] proposed a quantification of the interface temporal fluctuations, which they defined as the cohesive index. In our case, the interface temporal fluctuations will be used as the experimental dispersion qualitatively: if the averaged numerical interface is within the interface temporal fluctuations, then the model is sufficiently representative.

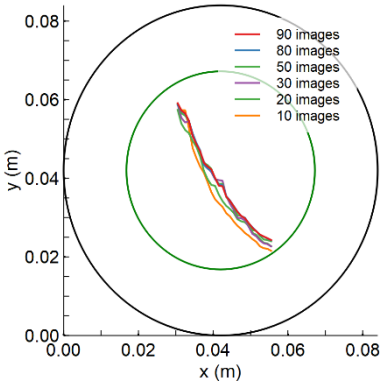

Figure 4: Influence of the number of images used on the average interface

To average coordinates of different lengths, the x-axis is divided in intervals of 1 mm. This allows a good resolution of the interface while having significant data (>1000) for each interval. Each coordinate is arranged in an interval according to its x-axis value. Finally, an averaged value of the y-axis is computed for each interval along the x-axis. This means that each x-axis value has a unique y-axis value associated with, and inversely, realising a bijection.

2.3.2. Extraction of the interface from CFD results and statistical comparison with experimental

Regarding the post-processing of the simulation, the interface was extracted at each written time of the simulation. To do so, a surface contour with a value of 5% regarding the solid volume fraction is performed. It means that the coordinates where the solid volume fraction is around 5% is extracted. This value was chosen as some air appears near the interface and having a limit of 5% gives less noise in the interface extraction. In order to have the same length of arrays as the experimental one, the same procedure described at the end of the section 2.3.1 was used.

The mean absolute error (MAE) and the root mean square error (RMSE) are used to evaluate the interface deviation. The MAE and RMSE calculation are respectively written in equations 3 and 4.

$$MAE = \frac{1}{n}\sum_{i=1}^{n}(y(x)_i - y(x)_i^*) \quad (3)$$

$$RMSE = \sqrt{\frac{1}{n}\sum_{i=1}^{n}(y(x)_i - y(x)_i^*)^2} \quad (4)$$

With $y(x)_i$ and $y(x)_i^*$ respectively the predicted and the experimental ordinate value for a given abscissa value and n the number of samples. In this study, the MAE is more appropriate as the size of dataset for the interface is relatively small (<100). However, the RMSE gives more weight to large errors and is better for revealing model performance differences [42]. Moreover, the RMSE cannot be determined from the MAE and inversely [43]. As the two measures are different but both relevant, MAE and RMSE are computed to measure the interface deviation.

3. CFD SIMULATIONS

3.1. Mesh and simulation conditions

The grid mesh used for CFD was performed using the software Pointwise®. The diameter of the mesh is 84 mm with a depth of 20 mm, which is equal to the geometry of the rotating drum (section 2.1). The cylindrical shape of the drum was meshed using the O-grid method while keeping cell non-orthogonality as low as possible using the software Pointwise® (Figure 5).

A mesh convergence was performed to investigate the influence of the number of cells contained in the mesh on the interface and on the U_x velocity with the dense granular flow model described in section 3.3 (Figure 5). Regarding the interface, the coarse meshes (cells equal or lower than 3825) are relatively different from fine mesh (cells equal or higher than 28050). Yet, the finer the mesh, the better the interface resolution as there are more cells in this region. However, there is not much difference between 28050, 213840 or 1689600 cells (Figure 5a).

Regarding the U_x velocity, the probe that extracts this value was placed at the same location for each mesh, near the wall (Figure 5c). It can be seen that the mesh has no influence on the velocity (Figure 5a). As the rotation speed is low (1 RPM), the flow is laminar, meaning that high mesh resolution is not needed. However, to have a sufficient resolution of the interface with an acceptable simulation time, a mesh of 231840 cells was selected. This mesh size was used for all simulation.

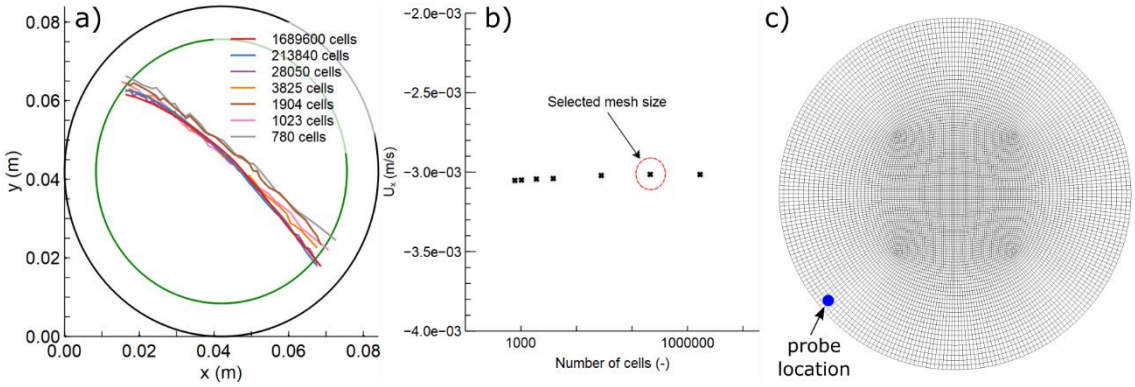

Figure 5: Mesh convergence with the dense granular flow model a) influence of the number of cells on the gas/solid interface, b) influence of the number of cells on the velocity in the x direction at 1 RPM and c) selected mesh size with the probe location

All the patches of the geometry mesh are considered as walls. Regarding the boundary conditions, the velocity at the wall has a movingWallVelocity condition, a condition used in OpenFoam for cases with moving walls, implying that the fluid touching the drum wall also has a no-slip boundary condition but the mesh vertices move with the surface. For the pressure, the boundary conditions set the pressure gradient to the provided value such that the flux on the boundary is that specified by the velocity boundary condition. For all other variables, a zero gradient at the drum wall is performed.

During the simulation, the whole mesh is rotating to a fixed value using the solid-body rotation (dynamic mesh) in OpenFoam. For the KTGF model, an adaptive time step was chosen with a maximum Courant–Friedrichs–Lewy number equal to 0.5. For the $\mu(I)$ law, as the powder starts to flow when the angle reaches the critical angle μ_s, the flow can be intermittent. An adaptive time step led to non-stable results, especially at the interface. Therefore, a fixed time step of 10^{-3} seconds was chosen. The pressure-velocity was solved using a PIMPLE algorithm. A reference pressure of zero is set at the middle-top of the drum. Each simulation was run for at least three drum revolutions.

The powder inside the drum was initialised with the setFields utility from OpenFoam. The drum filling degree for the simulation had to correspond with the experimental conditions. For

rice flour, some powder was stuck at the drum wall during the rotation (Figure 2b), modifying the actual filling degree. Indeed, the drum was originally 50% filled but around 5% of the powder was stuck at the drum wall away from the powder at rest at the end of the rotation. This 5% of the powder stuck at the drum wall also appears during the rotation, away from the dense powder flow (Figure 2b). This means that during the rotation, 95% of the powder actually flows in the rotating drum. As during the CFD simulation, no powder is getting stuck at the drum wall, the simulation for rice flour was initialised with a powder volume equal to 45% of the total drum volume in order to be closer to the experimental powder flow. For brown corundum F180 and for glass powder, the simulation was initialised with a powder volume equal to 50% of the total drum volume.

3.2. Kinetic theory of granular flow

The KTGF model is solved with multiphaseEulerFoam from OpenFOAM, a CFD multiphase solver. The solid and the gas phases are solved separately, using an Euler-Euler formulation. Mass conservation is written according to equation 5 [24,44].

$$\frac{\partial(\alpha_\varphi.\rho_\varphi)}{\partial t} + \nabla.\left(\vec{U}_\varphi.\alpha_\varphi\rho_\varphi\right) = 0 \quad (5)$$

With φ that denotes each phase, α the phase volume fraction, $\vec{U}$ the velocity and ρ the density. The momentum equation is given in equation 6.

$$\frac{\partial(\alpha_\varphi.\rho_\varphi.\vec{U}_\varphi)}{\partial t} + \nabla.\left(\alpha_\varphi\rho_\varphi\vec{U}_\varphi\,\vec{U}_\varphi\right) - \nabla.\tau_\varphi = -\alpha_\varphi.\nabla p + \alpha_\varphi\rho_\varphi\vec{g} + \vec{M}_\varphi + \vec{S}_\varphi \quad (6)$$

With τ the stress tensor, p the pressure, $\vec{g}$ the gravitational force, M is the rate of interfacial momentum transfer and S is the momentum source term [44]. The momentum source is equal to zero as this is a closed mesh without external circulation: no additional interaction appears with the rotating drum medium. The KTGF supposes instantaneous and binary collisions of particles [29,45]. This model introduces the granular temperature, which represents the energy fluctuation within the solid, noted Θ_s (equation 7) [29], where $\overrightarrow{C_s}$ is the random fluctuation velocity of the solid [24].

$$\Theta_s = \frac{1}{3}.<\overrightarrow{C_s}.\overrightarrow{C_s}> \quad (7)$$

The granular temperature intervenes in the calculation of the granular shear viscosity, noted μ_{gs}. This granular shear viscosity is the sum of three contributions (equation 8): the collision viscosity, noted $\mu_{gs,col}$, the kinetic viscosity, noted $\mu_{gs,kin}$, and the friction viscosity, noted $\mu_{gs,fr}$ [24,25].

$$\mu_{gs} = \mu_{gs,col} + \mu_{gs,kin} + \mu_{gs,fric} \quad (8)$$

For each shear viscosity contributions, there are many models to estimate it. van Wachem et al. [30] listed all the models for all the contributions. Here, no comparison is made between all these models: the most commons are selected. The collisional viscosity can be estimated with equation 9 while the kinetic viscosity can be calculated with equation 10, using the Gidaspow model.

$$\mu_{gs,col} = \frac{4}{5}.\alpha_s.\rho_s.d_p.g_0.(1+e).\left(\frac{\Theta_s}{\pi}\right)^{0.5} \quad (9)$$

$$\mu_{gs,kin} = \frac{10}{96}.\frac{\rho_s.d_p.(\Theta_s.\pi)^{0.5}}{g_0.(1+e).\alpha_s}.\left[1+\frac{4}{5}.\alpha_s.g_0.(1+e)\right] \quad (10)$$

With α_s the solid volume fraction, ρ_s the solid density, d_p the mean particle diameter, g_0 the radial distribution and e the restitution coefficient. The latter was fixed to 0.9 for each

simulation. The radial distribution is calculated with equation 11, from the Sinclair and Jackson model.

$$g_0 = \left(1 - \left(\frac{\alpha_s}{\alpha_{s,max}}\right)^{\frac{1}{3}}\right)^{-1} \quad (11)$$

With $\alpha_{s,max}$ the maximum solid volume fraction that can reach the solid. This value is fixed to $\alpha_{s,max} = 0.63$ [30,40]. This corresponds to the packed solid volume fraction at the beginning of the rotation. To do so, with the KTGF model, couple of seconds are waited before launching the rotation of the drum to reach the maximum packed solid volume fraction. The friction viscosity can be calculated with equation 12 using the Johnson and Jackson model [30].

$$\mu_{gs,fric} = \sin(\beta).Fr.\frac{\left(\alpha_s - \alpha_{s,min}^{fric}\right)^{b_1}}{\left(\alpha_{s,max} - \alpha_s\right)^{b_2}} \quad (12)$$

The friction contribution is added to the granular shear viscosity when the solid volume fraction exceeds $\alpha_{s,min}^{fric}$. This value is fixed to $\alpha_{s,min}^{fric} = 0.5$: the friction contribution appears for very dense gas-solid flow [30,46]. β is the angle of internal friction. For the Johnson and Jackson model, Fr, b_1 and b_2 are constant. In this study, they were respectively fixed to 0.05, 2 and 5.

3.3. Dense granular flow model

Before this study, the KTGF model was already implemented in the multiphase Euler solver. As the dense granular flow model was not implemented in any solver, it has been done for the VOF solver (interFoam from OpenFOAM), as the solid and the air phases are well separated. interFoam treats the solid and the air phases together as a mixture. The mass conservation is calculated with equation 13 [47].

$$\frac{\partial \rho_\varphi}{\partial t} + \nabla\left(\rho_\varphi . U\right) = 0 \quad (13)$$

With ρ the density and U the velocity. The density ρ is defined as equation 14.

$$\rho_\varphi = \alpha\rho_1 + (1-\alpha)\rho_2 \quad (14)$$

With α the volume fraction of the phase equal to 1 if a mesh cell is full of fluid with a density ρ_1 and equal to 0 if it is full of fluid with a density ρ_2. In order to get the interface between the two fluids, the equation 15 is solved.

$$\frac{\partial \alpha}{\partial t} + \nabla(\alpha U) = 0 \quad (15)$$

The momentum equation is calculated from equation 16.

$$\frac{\partial\left(\rho_\varphi . U\right)}{\partial t} + \nabla\left(\rho_\varphi . U . U\right) = -\nabla p + \nabla(\eta(\nabla U + \nabla U^T)) + \rho_\varphi g + f_{\sigma_i} \quad (16)$$

With η is the effective viscosity of the fluid. $f_{\sigma i}$ is the surface tension, which is equal to 0 in this study. The dense granular flow model is based on the Mohr-Coulomb law (equation 17), where τ is the shear stress, P is the isotropic pressure (normal stress) and c is the cohesion of the powder.

$$\tau = \mu(I).P + c \quad (17)$$

The friction coefficient $\mu(I)$, which depends on the inertial number I, can be calculated with equation 18, where μ_s and μ_2 are critical values respectively for low I values (*e.g.* low shear rate) and high I values (*e.g.* high shear rate), I_0 is a constant, $\dot{\gamma}$ is the shear rate, d_p is the mean particle diameter and ρ_s is the particle density [34].

$$\mu(I) = \mu_s + \frac{\mu_2 - \mu_s}{I_0/I + 1}$$
$$I = \frac{\dot{\gamma}.d_p}{\sqrt{P/\rho_s}} \quad (18)$$

Jop et al. [34] proposed a 3D generalisation of the friction law. The solid flow can be described as an incompressible fluid where internal stress tensor can be calculated with equation 19 [34,48], where $\dot{\gamma}_{ij}$ is the strain rate tensor, $|\dot{\gamma}|$ is the second invariant of $\dot{\gamma}_{ij}$ and $\eta(|\dot{\gamma}|, P)$ is the effective viscosity.

$$\sigma_{ij} = -P\delta_{ij} + \tau_{ij}$$
$$\tau_{ij} = \eta(|\dot{\gamma}|, P).\dot{\gamma}_{ij} \quad (19)$$
$$\eta(|\dot{\gamma}|, P) = \mu(I).\frac{P}{|\dot{\gamma}|}$$

Yet, as the solid starts to flow when $|\tau| > \mu_s.P$ [34], a maximum viscosity η_{max} has to be specified. It means that the solid viscosity is between $\eta(|\dot{\gamma}|, P)$ and the η_{max} value. To ensure that η_{max} is well specified, the solid part that flows must have an effective viscosity much lower than η_{max} (at least 10^2 times lower). Such method has been used for dense solid flow using VoF [37]. In this study, η_{max} was set to 0.1 Pa.s.

The model proposed by Jop et al. does not calculate the cohesion of the powder ($c = 0$). It means that this model should only be used for non-cohesive powders. During this work, modifications of the implemented model were done to take into account the cohesion of the powder c, especially for rice flour.

3.3.1. Cohesion of the powder – Berger model

In order to take into account the cohesion of the powder, the model proposed by Berger et al. [49] was investigated, by computing the term c (equation (17)) and introducing an adhesion index, noted η_{adh} and calculated according to equation (20).

$$\eta_{adh} = \frac{f_c}{P.d_p} \quad (20)$$

Where f_c is the adhesion force. The greater the adhesion index, the more cohesive the powder. Using this index, the inertial number is modified, noted I_c, according to equation (21) and the cohesion of the powder c is calculated according to equation (22).

$$I_c = \frac{I}{(1 + \alpha_0.\eta_{adh})^{1/2}} \quad (21)$$

$$c = \frac{k_0.\eta_{adh}.P}{1 - \beta_0.\ln(1 - I_c)} \quad (22)$$

Where α_0, β_0 and k_0 are constants ($\alpha_0 = 0.08$, $\beta_0 = 6.4$ and $k_0 = 0.02$) taken from [49]. The modified inertial number is replaced in equation 18 and the cohesion of the powder is added to equation 19, resulting in equation (23), with η_c the modified effective viscosity.

$$\eta_c(|\dot{\gamma}|, P) = \frac{\mu(I_c).P + c}{|\dot{\gamma}|} \quad (23)$$

The results with the Berger model will be discussed later. For now, only the results with the model proposed by Jop et al. will be presented.

4. RESULTS AND DISCUSSIONS

4.1. Experimental results obtained from the rotating drum

The results obtained from the GranuDrum™ are displayed in Table 2. All the experiments were repeated at least 5 times. The relative standard deviation, calculated as the sample standard deviation equation, of each measured parameter is below 15%. If we estimate the Reynolds number adapted for rotating geometry such as $Re = \rho.N.D^2/\mu$ [50,51], with $\rho = 1815$ kg.m-3 (maximum ρ_{bulk}, Table 1) and $\mu = 10^{-3}$ Pa.s (viscosity relatively lower than the studied powder), the maximum Reynolds number at 10 RPM is $Re_{max} = 2134$. This means that the studied flow regime is always laminar, even by overestimating the Reynolds number. The Froude number, calculated as $Fr = (\omega^2.(D/2)/g)$ where ω is the angular rotation speed in rad/s, is lower than 1×10^{-4} for 1 RPM which corresponds to the surging regime, lower than 10^{-3} for 4 RPM which corresponds to the rolling regime. From 6 to 10 RPM, it is in between the rolling and the cascading regimes [7].

Table 2: Results obtained from the GranuDrum™ for different powder and rotation speeds

		Brown corundum F180		Glass powder		Rice flour	
Rotation speed (RPM)	Fr (-)	Angle (°)	Cohesive index (-)	Angle (°)	Cohesive index (-)	Angle (°)	Cohesive index (-)
1	$4.70.10^{-5}$	35.14±0.38	4.27±0.37	44.32±0.82	9.90±1.39	58.52±2.59	39.60±5.78
2	$1.88.10^{-4}$	36.33±0.40	4.65±0.15	44.67±0.75	9.59±0.83	56.54±2.64	38.02±6.47
4	$7.51.10^{-4}$	37.35±0.35	5.30±0.16	44.11±0.59	9.11±0.54	55.83±2.38	36.72±5.49
6	$1.69.10^{-3}$	39.16±0.69	9.00±0.31	45.09±0.39	13.51±1.42	57.09±1.70	40.98±4.20
8	$3.00.10^{-3}$	40.89±0.88	10.14±0.49	46.67±1.19	14.02±1.01	57.47±2.00	42.23±3.02
10	$4.70.10^{-3}$	40.61±0.32	10.92±0.57	49.25±1.30	15.78±0.91	56.91±1.86	43.51±3.24

First, it can be seen that increasing the rotation speed of the rotating drum also increase the dynamic angle of repose. As the rotation increases, the shear rate at the wall is enhanced, which causes the powder to be more lifted up in the rotation direction. Moreover, the cohesive index also increases with the rotation speed. As more shear stress is undergone inside the powder, the interface is less stable, leading to more fluctuations at the interface.

Regarding rice flour, the dynamic angle of repose θ_D is similar, no matter the rotation speed. Such results are in agreement with cohesive powders inside a rotating drum [8]. As explained before, from images recorded, it can be seen that some rice flour is stuck within the drum, especially near the wall (Figure 2b). This is not the case with a good powder flowability (Figure 2a). It means that rice flour is not able to freely flow inside the drum. From a previous study, the minimum orifice diameter for rice flour to flow has been measured with the Flodex apparatus [52]. Rice flour is able to freely flow when the diameter is 26 mm, which is larger than the depth of the rotating drum (L=20 mm). This explains why the dynamic angle of repose does not vary with the rotation speed.

From Table 1, brown corundum F180 is more flowable than glass powder, and glass powder is more flowable than rice flour (lower Hausner and lower static angle of repose, Table 1). It can be seen that θ_D and CI depends on the powder flowability. The better the powder flowability, the lower the θ_D and the CI. If a powder has a good flowability, the powder viscosity is lower, meaning that the angle taken by the interface slope is reduced. Moreover, if a powder has a lower flowability, its flow will be intermittent, which will lead to higher fluctuations of the interface. This is particularly the case for rice flour, which presents a chaotic flow as it is cohesive [10,52].

The interface coordinates were extracted for each rotation speed and powder studied. Figure 6 displays all the interface coordinates taken by the powder during the rotations (grey) and the average interface coordinates (blue, named "Av. Exp"). It can be seen that, with non-cohesive powder, all the interface coordinates are close to the average (Figure 6a and b). This is in agreement with the low cohesive index measured with brown corundum F180 (Table 2). Yet, for cohesive powder, the interface coordinates change strongly during the rotation. Indeed, some interface coordinates are quite different to the average (Figure 6c and d). This shows the chaotic flow of cohesive powder, giving a large spread of the interface coordinates. This is also in agreement with the larger value of the cohesive index measured with rice flour (Table 2). Moreover, the average interface for rice flour are quite similar for 1 and 10 RPM (Figure 6c and d).

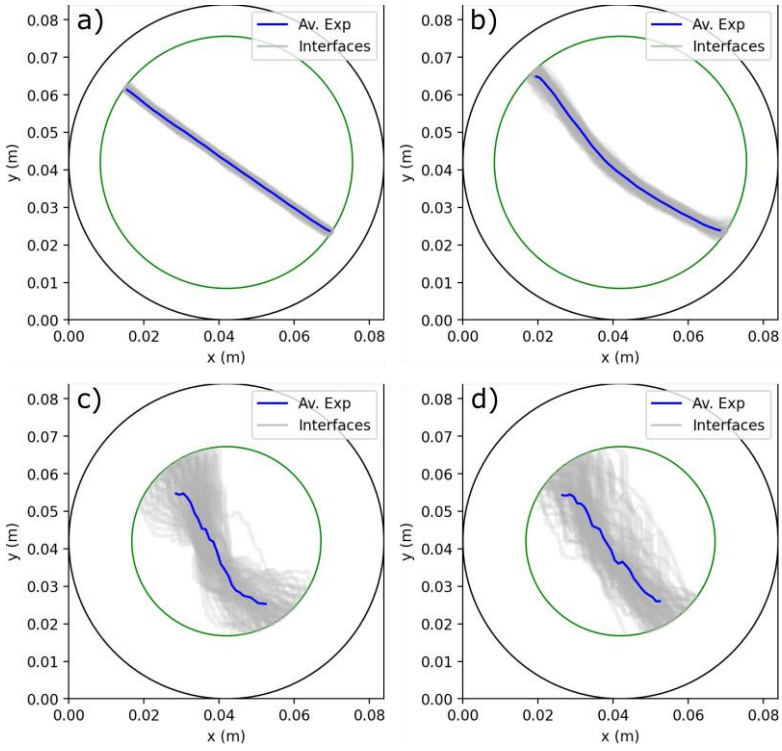

Figure 6: All interface coordinates and averaged interface coordinates with brown corundum F180 at a) 1 RPM and b) 10 RPM and with rice flour at c) 1 RPM and d) 10 RPM. The interfaces in grey are the experimental interface fluctuations.

Having all the interface coordinates and the average allows comparing these curves with the ones obtained from CFD. The two models presented in sections 3.2 and 3.3 will be compared with the experiments. The CFD model is validated if the interface coordinates from numerical simulations match with the experiment, taking into account the dispersion of the interface coordinates during the experiment.

4.2. Comparison of experiments with CFD results

4.2.1. The KTGF Model

Model parameters for the KTGF model are listed in Table 3. The ρ_s and the d_p values were measured experimentally. e, $\alpha_{s,max}$ and $\alpha_{s,min}^{fric}$, were fixed according to the values usually taken in the literature [24,25]. The values are specified in section 3.2. The d_p values correspond to the Sauter diameter (d_{32}), listed in Table 1.

Table 3: Parameters for the KTGF model

	Brown corundum F180	Glass powder	Rice flour
ρ_s (kg.m^{-3})	3025	1540	915
d_p (µm)	66.5	61.6	39.2

The results obtained from the KTGF model are displayed on Figure 7 with brown corundum F180. It can be seen that, for low RPM (less than or equal to 2 RPM, corresponding to the surging regime), the KTGF model does not represent the experimental interface (Figure 7a) while for high RPM (higher than or equal to 4 RPM, corresponding to rolling and cascading regime), the simulation and the experiment are a bit closer (Figure 7b), but some deviations still exist.

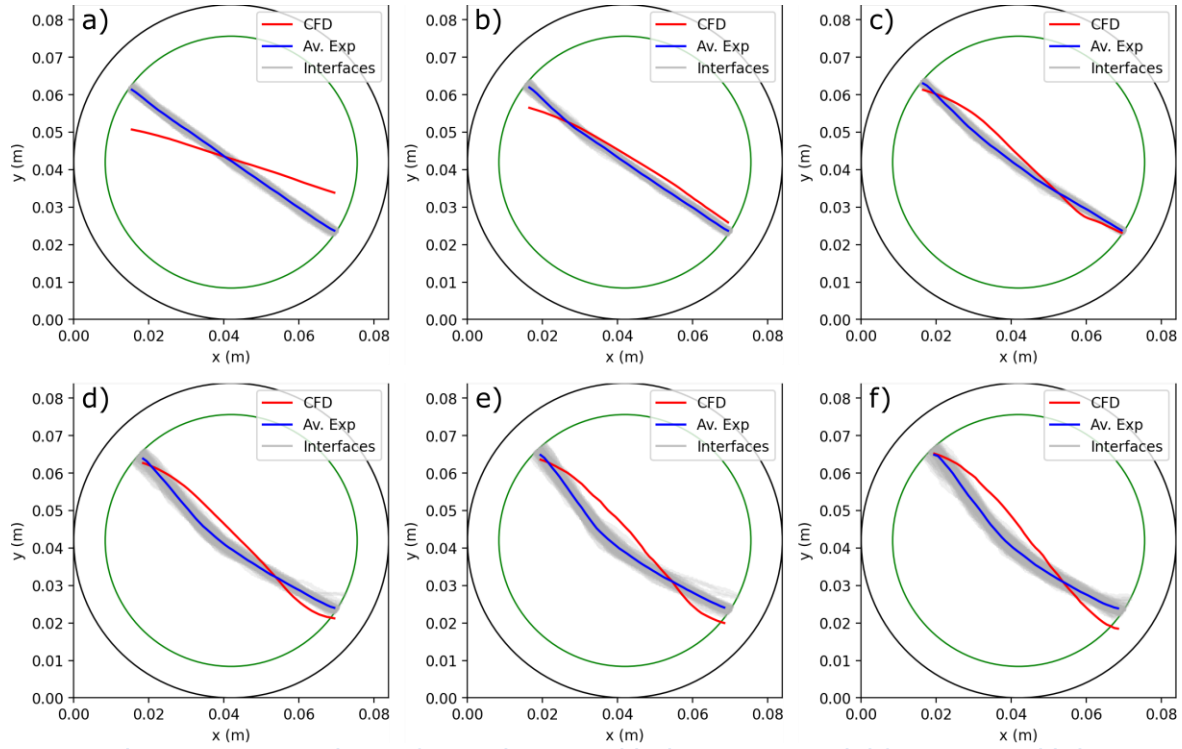

Figure 7: Comparison of experiments with the KTGF model from CFD with brown corundum F180 at a) 1 RPM, b) 2 RPM, c) 4 RPM, d) 6 RPM, e) 8 RPM and f) 10 RPM. The interfaces in grey are the experimental interface fluctuations. The simulated results from CFD in red corresponds to average value.

The interfaces obtained with the KTGF model for glass powder are illustrated on Figure 8. Here again, for low rotation speed, the KTGF model fails to represent the powder rheology. For 4 RPM and higher, there is a close match between averaged experiments and the CFD model.

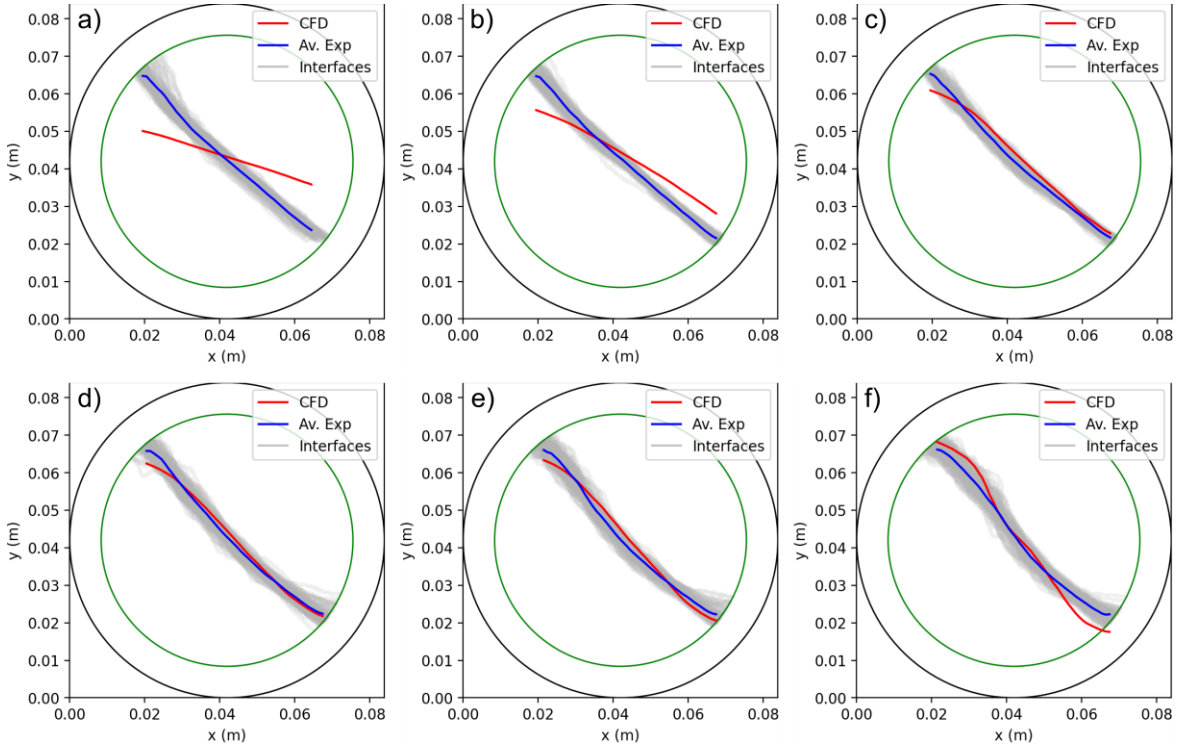

Figure 8: Comparison of experiments with the KTGF model from CFD with glass powder at a) 1 RPM, b) 2 RPM, c) 4 RPM, d) 6 RPM, e) 8 RPM and f) 10 RPM. The interfaces in grey are the experimental interface fluctuations. The simulated results from CFD in red corresponds to average value.

Finally, the comparison between the KTGF model and the experiment with rice flour is displayed on Figure 9. Here, the averaged experimental interfaces are calculated over a narrower area than the cropped region, as there are fewer interface coordinate points at the extremities of the cropped region. Thus, taking those extremity points would create a bias on the interface average. Moreover, the CFD interface range must coincide with the averaged experimental interfaces to compare them. Once again, the model does not match the experimental interface for 2 RPM or lower. A better match appears for 4 RPM but for higher rotation speeds, the CFD model shows different bed shape compared to experiment. Indeed, a small plateau appears for $x \geq 0.04$ m. According to Geldart classification of particles [39], rice flour belongs to the group A (small mean size and/or low density, Table 1). Wheat flour, akin to rice flour, behaves like a group C category [53]. However, an unmodified KTGF model is not adapted for group A particles [54], as it does not take into account cohesion between particles [55]. This should be even worse for group C particles, explaining here the difficulty to model the interface.

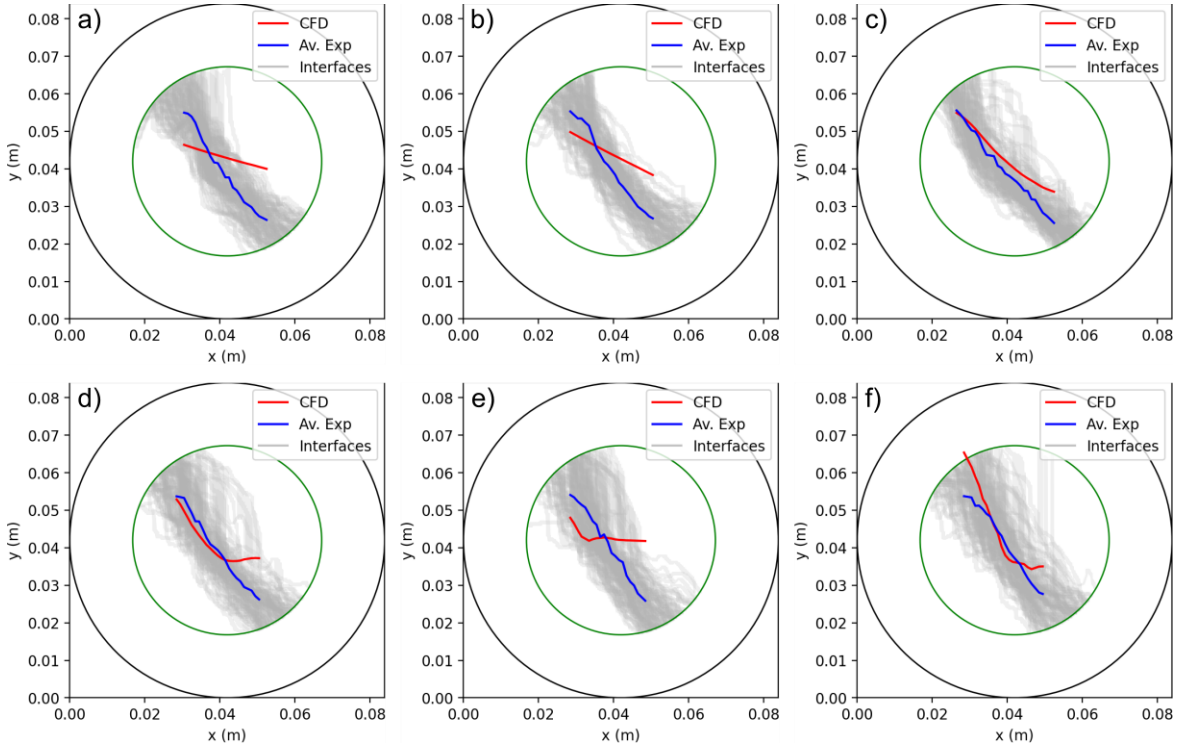

Figure 9: Comparison between experiments and the KTGF model from CFD with rice flour at a) 1 RPM, b) 2 RPM, c) 4 RPM, d) 6 RPM, e) 8 RPM and f) 10 RPM. The interfaces in grey are the experimental interface fluctuations. The simulated results from CFD in red corresponds to average value.

The interface fluctuations over time from CFD simulations with the KTGF model are plotted in Figure 10. It can be seen that there are low fluctuations with brown corundum F180 (Figure 10a and b), even at 10 RPM, compared to experimental results (Figure 6a and b). For rice flour, no numerical interface fluctuations appears at 1 RPM (Figure 10c), whereas the interface fluctuates a lot experimentally at 1 RPM (Figure 6c). At 10 RPM with rice flour, the interface fluctuates more compared CFD results at 1 RPM (Figure 10d). However, these numerical interface fluctuations are not as intense as the ones obtained experimentally (Figure 6d). In any case, the KTGF model does not represent well the interface fluctuations obtained experimentally.

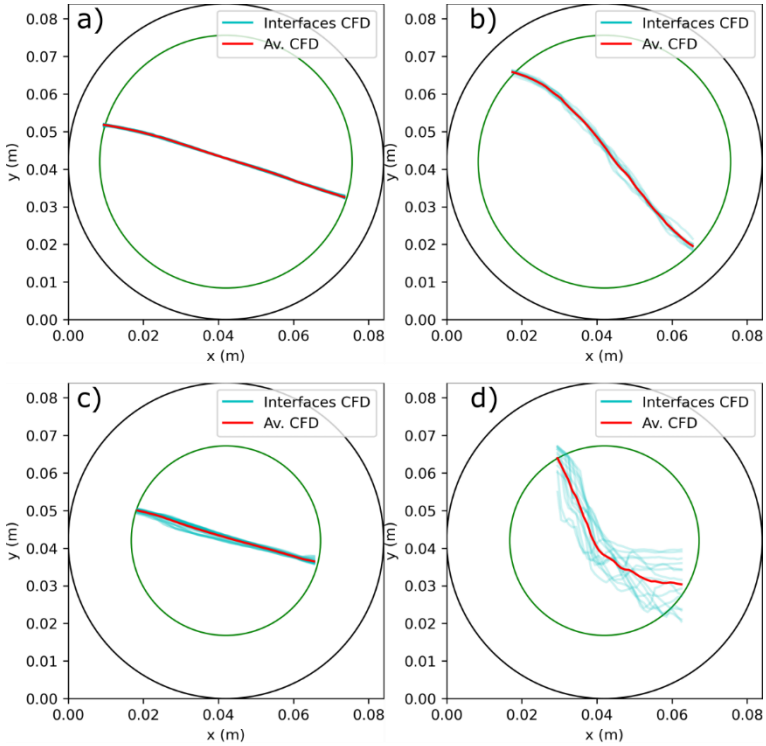

Figure 10: Interface fluctuations over time from CFD simulations using the KTGF model with brown corundum F180 at a) 1 RPM and b) 10 RPM and with rice flour at c) 1 RPM and d) 10 RPM. The interfaces in cyan are the numerical interface fluctuations.

To have a quantitative result on the interface fluctuations over time from CFD simulations, the cohesive index (equation (1)) was calculated for each simulation obtained with the KTGF model (Table 4). The cohesive index increases with the rotation speed, especially with rice flour, and decreases with better powder flowability, but not as much as in the experiments (Table 2). Moreover, the cohesive index obtained numerically is significantly lower compared to experiments: the interface fluctuations obtained from CFD with the KTGF model does not represent the experimental fluctuations.

Table 4: Cohesive index calculated with the KTGF model.

RPM	Fr (-)	Brown corundum F180	Glass powder	Rice flour
1	$4.70.10^{-5}$	1.18	0.88	2.70
2	$1.88.10^{-4}$	1.18	1.14	4.72
4	$7.51.10^{-4}$	4.05	6.01	6.20
6	$1.69.10^{-3}$	3.40	6.24	7.05
8	$3.00.10^{-3}$	2.38	4.53	12.03
10	$4.70.10^{-3}$	1.62	4.19	12.80

Table 5 lists the statistical analysis for the comparison between the KTGF model and the experiments. It can be seen that the highest value for the MAE and RMSE is always at 1 RPM, indicating a deviation of the model compared to the experiment. This is in agreement with Figure 7a, Figure 8a and Figure 9a.

Moreover, for each powder, there seems to be an optimum on the MAE and RMSE values. The optimum seems to appear at around 4 or 6 RPM. This corresponds to the best match obtained between CFD and experiments (see Figure 7c for brown corundum F180,

Figure 8d for glass powder and Figure 9c for rice flour). This shows that the statistical analysis is in agreement with the visualisation of the displayed figures. The KTGF model is more adapted for well-agitated medium.

Table 5: MAE and RMSE between experiments and the KTGF model from CFD for brown corundum F180, glass powder and rice flour at speed 1, 2, 4, 6, 8 and 10 RPM

		Brown corundum F180		Glass powder		Rice flour	
Rotation speed (RPM)	Fr (-)	MAE (mm)	RMSE (mm)	MAE (mm)	RMSE (mm)	MAE (mm)	RMSE (mm)
1	$4.70.10^{-5}$	5.23	6.05	6.80	8.01	7.07	8.07
2	$1.88.10^{-4}$	2.29	2.25	4.15	4.82	6.13	6.94
4	$7.51.10^{-4}$	2.26	2.67	1.79	1.99	3.34	4.08
6	$1.69.10^{-3}$	3.32	3.76	1.18	1.48	3.67	4.73
8	$3.00.10^{-3}$	4.23	4.86	1.65	1.84	6.85	7.98
10	$4.70.10^{-3}$	4.62	5.28	2.53	3.03	3.62	4.78

4.2.2. The dense granular flow model

The parameters for the dense granular flow model are listed in Table 6. It can be seen that the μ_s and μ_2 parameters are directly taken from the experimental results obtained with the GranuDrum™ (Table 2). Indeed, μ_s and μ_2 respectively correspond to the lowest and the largest dynamic angle of repose values measured with the GranuDrum™ for a given powder. The I_0 parameter is a constant, for which the order of magnitude is around 0.3 [34,49]. Here again, the d_p values correspond to the d_{32} displayed in Table 1.

Table 6: Parameters for the dense granular flow model

	Brown corundum F180	Glass powder	Rice flour
ρ_s (kg.m-3)	3025	1540	915
μ_s (-)	$\tan(35.14)$	$\tan(44.32)$	$\tan(55.83)$
μ_2 (-)	$\tan(40.61)$	$\tan(49.25)$	$\tan(58.52)$
I_0 (-)	0.3	0.3	0.3
c (Pa)	0	0	0
d_p (µm)	66.5	61.6	39.2

The results obtained from the dense granular flow model with brown corundum F180 are displayed on Figure 11. In this case, the granular flow model represents accurately the powder shape taken in a rotating drum, even for low RPM. The model captures the elbow shape appearing at 6, 8 and 10 RPM for x≈0.04 m (Figure 11a, b and c). The dense granular flow seems to be suitable for non-cohesive powders.

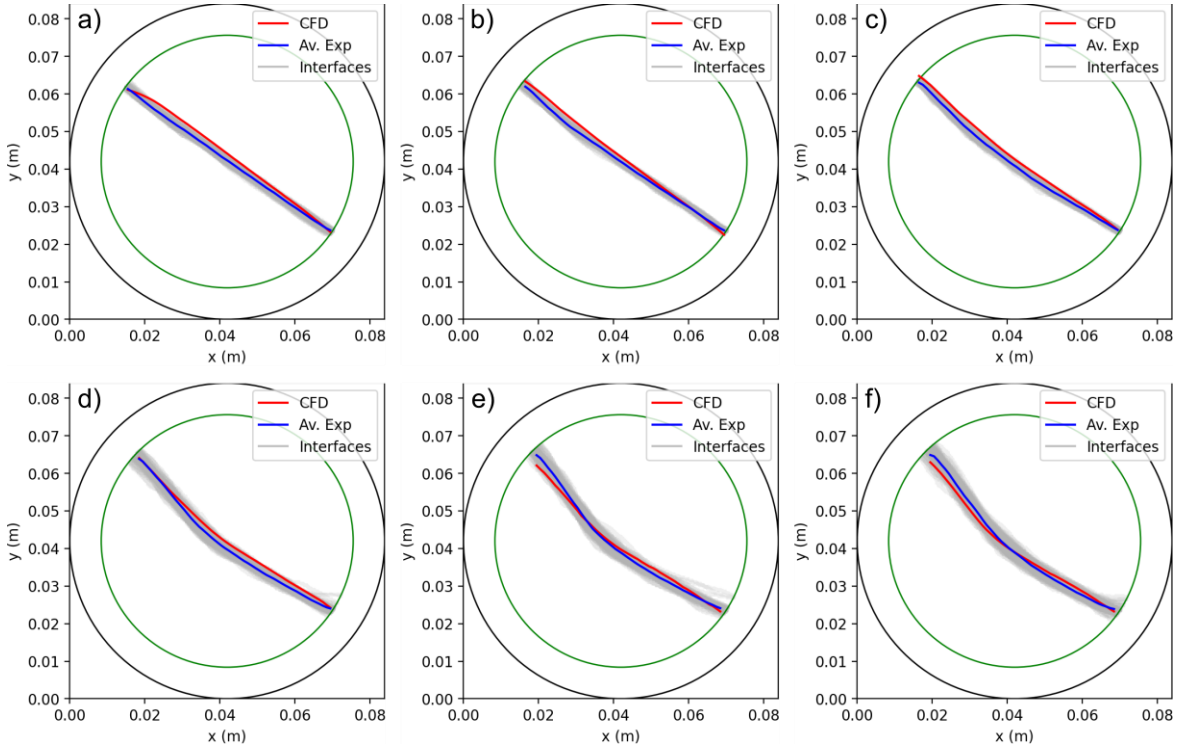

Figure 11: Comparison between experiments and the dense granular flow model from CFD with brown corundum F180 at a) 1 RPM, b) 2 RPM, c) 4 RPM, d) 6 RPM, e) 8 RPM and f) 10 RPM. The interfaces in grey are the experimental interface fluctuations. The simulated results from CFD in red corresponds to average value.

The comparison between dense granular flow model and experiment for glass powder is illustrated on Figure 12. Here, the CFD is close to the averaged experimental interface for rotation speeds equals to 6 RPM or lower (Figure 12a, b and c). A small deviation appears for higher rotation speeds. In general, there is a good agreement between CFD and experiment for any studied rotation speed.

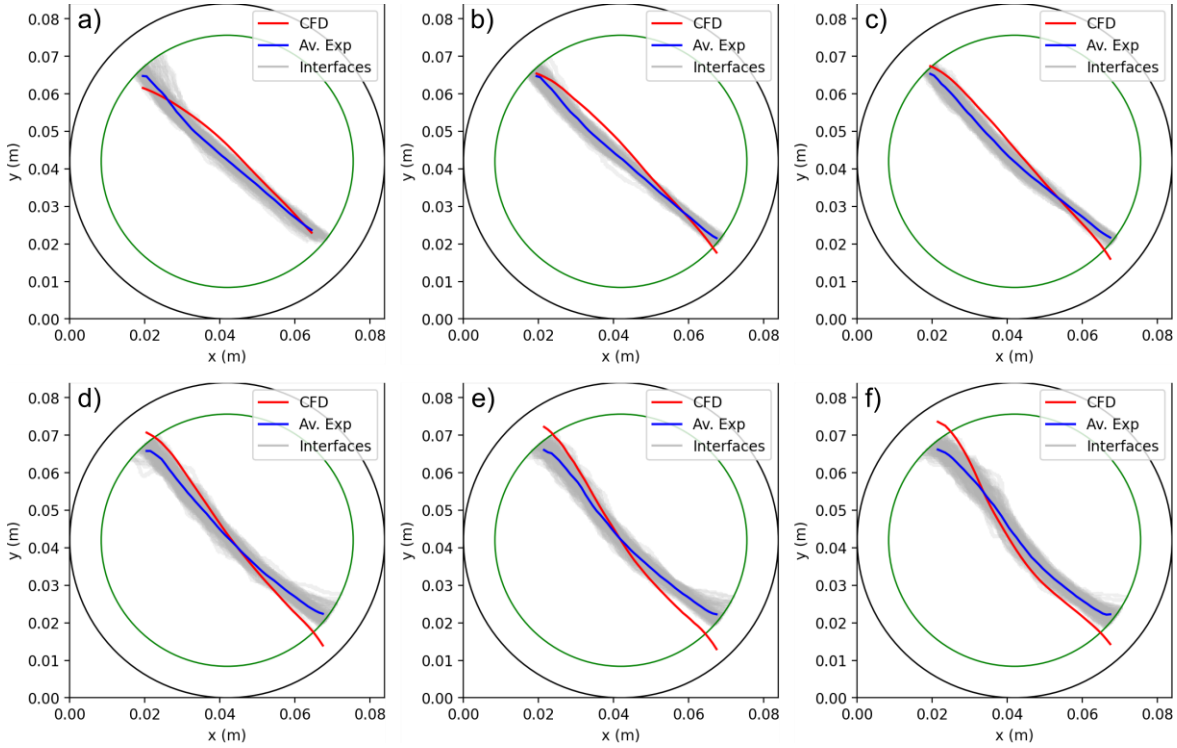

Figure 12: Comparison between experiments and the dense granular flow model from CFD with glass powder at a) 1 RPM, b) 2 RPM, c) 4 RPM, d) 6 RPM, e) 8 RPM and f) 10 RPM. The interfaces in grey are the experimental interface fluctuations. The simulated results from CFD in red corresponds to average value.

Finally, Figure 13 illustrates the comparison with the dense granular flow model and the experiment with rice flour. Here, the CFD interface is relatively close to the average experimental interface. Moreover, the CFD interface is within the experimental interface fluctuation (in grey). This shows that the dense granular flow, developed for non-cohesive powders [34] (cohesion of the powder $c = 0$, equation 17), can capture the rheology of rice flour, even for powder being relatively cohesive [4]. This may not be the case for more cohesive powder. In the light of the above considerations, it would be beneficial to incorporate an extension to the Jop model that takes account of powder cohesion.

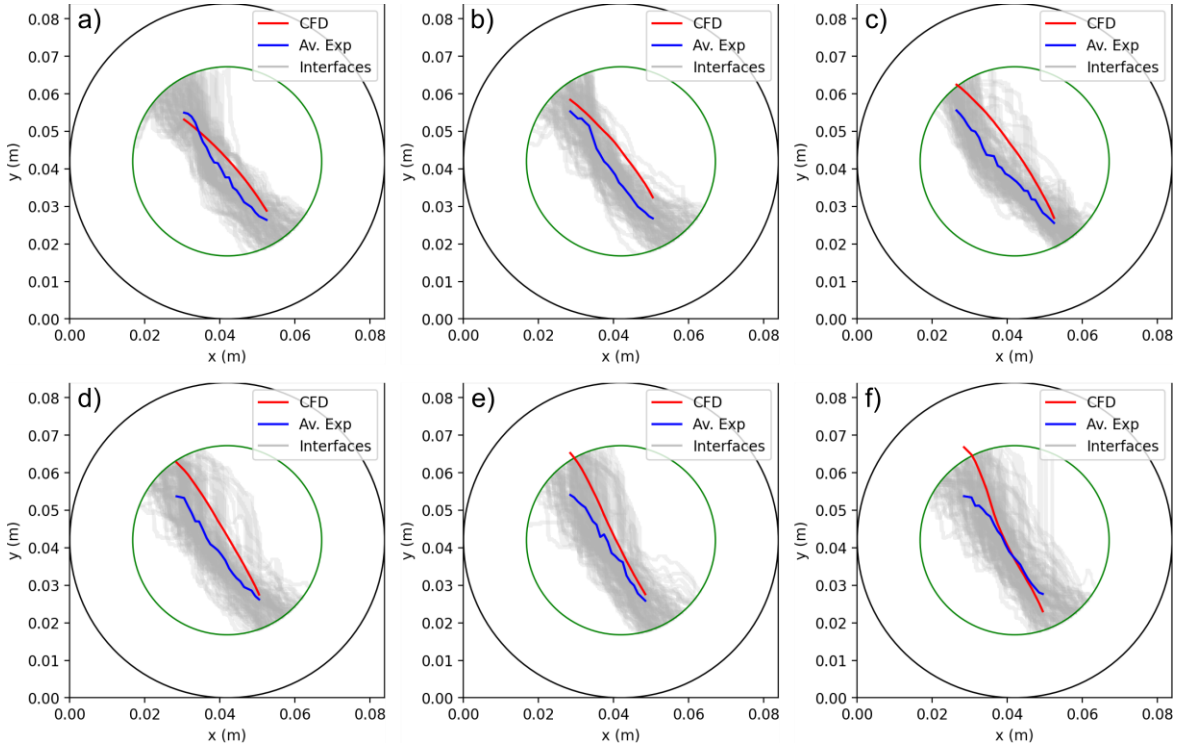

Figure 13: Comparison between experiments and the dense granular flow model from CFD with rice flour at a) 1 RPM, b) 2 RPM, c) 4 RPM, d) 6 RPM, e) 8 RPM and f) 10 RPM. The interfaces in grey are the experimental interface fluctuations. The simulated results from CFD in red corresponds to average value.

Figure 14 illustrates the interface fluctuations obtained with the dense granular flow model. Here, the same conclusion from Figure 10 can be done. The dense granular flow model fails to represent the interface fluctuations when compared with the experiment ones (Figure 6), even at 10 RPM and with rice flour. From the dense granular flow model, there is no term that takes into account the flow intermittences.

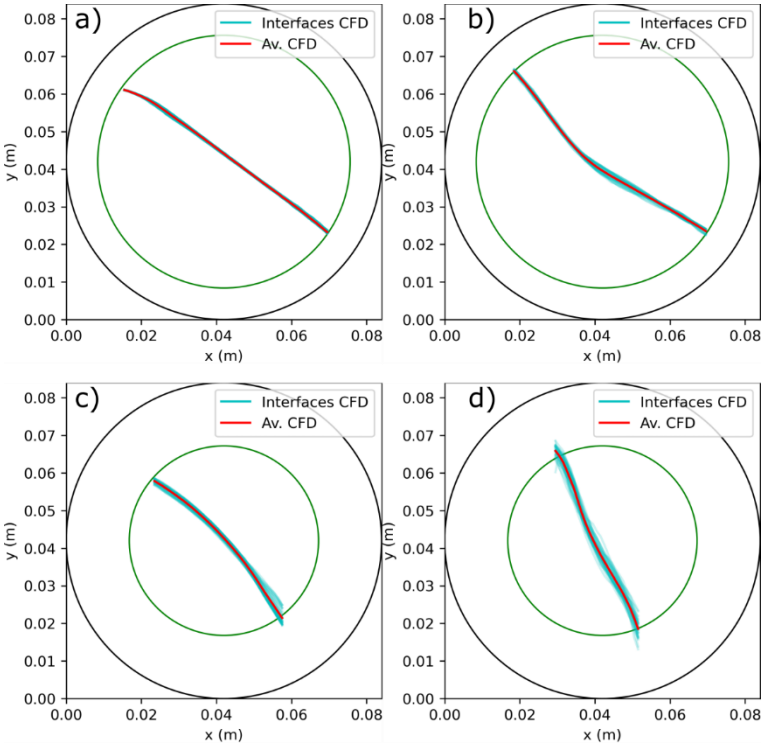

Figure 14: Interface fluctuations over time from CFD simulations using the dense granular flow model with brown corundum F180 at a) 1 RPM and b) 10 RPM and with rice flour at c) 1 RPM and d) 10 RPM. The interfaces in cyan are the numerical interface fluctuations.

The cohesive indices obtained from CFD with the dense granular flow model are listed in Table 7. Compared with the KTGF model (Table 4), the dense granular flow model shows higher interface fluctuations for low rotation speeds (equal or lower than 2 RPM) but the inverse appears for high rotation speeds (equal or higher than 4 RPM). Akin to the cohesive indices obtained with the KTGF model, the ones obtained with the dense granular flow model are considerably lower compared to experimental data (Table 2). The CFD models give an average flow of the powder inside the rotating drum.

Table 7: Cohesive index calculated with the dense granular flow model

RPM	Fr (-)	Brown corundum F180	Glass powder	Rice flour
1	$4.70.10^{-5}$	1.35	3.97	6.27
2	$1.88.10^{-4}$	1.36	4.93	9.09
4	$7.51.10^{-4}$	1.95	4.48	4.71
6	$1.69.10^{-3}$	2.28	4.61	5.57
8	$3.00.10^{-3}$	2.13	5.12	5.51
10	$4.70.10^{-3}$	1.97	4.74	5.09

Table 8 lists the MAE and RMSE results between the dense granular flow model and the experiments. For any rotation speed, decreasing the powder flowability increases the MAE and RMSE, meaning that the CFD model is better for good powder flowability. This is in agreement with section 3.3: the dense granular flow model best corresponds to non-cohesive solids flow. More CFD comparison with experimental results should be conducted to investigate the reliability of the dense granular flow model for different powder properties (e.g. density, diameter, and so on).

Table 8: MAE and RMSE between experiments and the dense granular flow model from CFD for brown corundum F180, glass powder and rice flour at speed 1, 2, 4, 6, 8 and 10 RPM

		Brown corundum F180		Glass powder		Rice flour	
Rotation speed (RPM)	Fr (-)	MAE (mm)	RMSE (mm)	MAE (mm)	RMSE (mm)	MAE (mm)	RMSE (mm)
1	$4.70.10^{-5}$	1.445	1.591	2.432	2.758	3.881	4.233
2	$1.88.10^{-4}$	1.236	1.442	2.754	3.195	6.621	7.039
4	$7.51.10^{-4}$	1.619	1.706	2.941	3.277	7.260	7.646
6	$1.69.10^{-3}$	1.328	1.471	3.304	3.822	7.302	7.640
8	$3.00.10^{-3}$	1.093	1.292	3.930	4.417	6.203	6.859
10	$4.70.10^{-3}$	1.157	1.369	4.062	4.399	4.159	5.902

A small trend appears on the increase of the MAE and RMSE value with the increase of the rotation speed, especially for glass powder and rice flour. It may indicate that the powder rheology is more difficult to capture at higher shear rate and for less flowable powder. As explained in section 3.3.1, the Berger model was used for taking into account cohesion of the powder. The results are displayed in Figure 15.

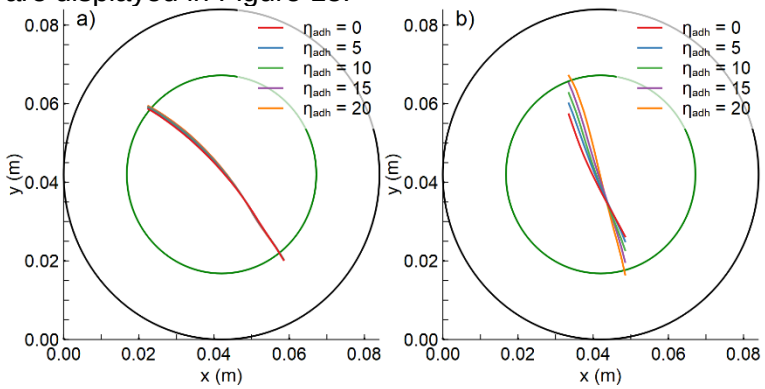

Figure 15: Influence of the adhesion index from the Berger model [49] with rice flour at: a) 1 RPM and b) 10 RPM

It can be seen that, for a low rotation speed (1 RPM, Figure 15a), the adhesion index has no influence on the average interface. Yet, for a higher rotation speed (10 RPM, Figure 15b), increasing the adhesion index also increases the effective viscosity as the average interface is steeper. For a given shear rate (i.e. rotation speed), the modified inertial number I_c is lower for a higher adhesion index (equation (21)). Thus, increasing the adhesion index diminishes the denominator and increases the numerator in equation (22), which increases the cohesion of the powder and thus the effective viscosity (equation (23)). Lowering the modified inertial number I_c should also reduce the friction coefficient $\mu(I)$. However, the cohesion of the powder scales faster compared to the friction coefficient due to the negative logarithm in the denominator of equation (22). For very low rotation speed, the effective viscosity has minimum influence on the interface shape: the contribution of the cohesion of the powder c in the effective viscosity calculation (equation (23)) is negligible.

The cohesive index was also calculated for different adhesion indices at 1 RPM and at 10 RPM with rice flour Table 9. It can be seen that increasing the adhesion η_{adh} reduces the cohesive index for 1 RPM. Yet, for 10 RPM, the cohesion index is modestly increased with the

increase of the adhesion index. In any case, the cohesion index obtained numerically is still much lower than the ones obtained experimentally (Table 2). Therefore, the Berger model does not represent adequately the rheology of cohesive powder.

Table 9: Influence of the adhesion index on the cohesive index with rice flour at 1 RPM and at 10 RPM

η_{adh}	CI at 1 RPM (-)	CI at 10 RPM (-)
0	6.27	5.09
5	5.28	6.25
10	4.21	6.88
15	3.27	8.64
20	2.96	8.00

4.3. Comparison between the two CFD models

For low rotation speed, equal or lower to 2 RPM, and non-cohesive powders (glass powder and brown corundum F180), the dense granular flow model gives the smallest MAE and RMSE values compared to the KTGF model. For higher rotation speed, the KTGF model is closer to the experiments with a lower MAE and RMSE for glass powder, but not for brown corundum F180.

Regarding rice flour, the dense granular flow model presents lower MAE and RMSE for low rotation speed. At high rotation speeds, the dense granular flow model gives average interfaces relatively close to experiments, while the KTGF model gives unrepresentative average interfaces with a plateau between the middle and the drum wall. The errors measured with MAE and RMSE are higher for both models than with brown corundum F180 and glass powder. For relatively cohesive powder, both models struggle to capture the powder rheology. As mentioned earlier, cohesive models are proposed for the dense granular flow [49,56,57]. Only the Berger et al. [49] model was tested for rice flour, without success. The contribution of the cohesive force in the $\mu(I)$ law is necessary for highly cohesive powder. To our knowledge, no reliable cohesive contribution model, as reliable as the Jop model, exists in the literature and it is still under research [56–58].

The reason why the KTGF model fails to represent the granular flow for low rotation speed is because it is based on instantaneous binary collisions [29]. This assumption is adapted for homogeneous gas-solid flow (*i.e.*, for uniform dilute and moderate dense solid concentration flow) [46], but not for heterogeneous gas-solid flow (*i.e.*, denser solid concentration flow, with clusters of dense solids flow and clusters of low solids concentration) [59]. The latter gas-solid flow can be treated by considering a combination of dilute and dense solid concentrations, and describing each phase with the KTGF model [60]. The former flow regime corresponds to the “gaseous” regime, where the medium is strongly agitated and the particle are far from each other [2]. This “gaseous” regime is not representative of the powder flow inside a rotating drum and even less for low rotation speed.

With the KTGF, the viscosity of the solid depends on the granular temperature. The granular temperature is linked to the velocity fluctuation (equation (7)). For low rotation speed, the velocity fluctuations are negligible, which leads to low granular temperature and thus to low solid viscosity. Wu et al. [61] listed different ways to improve the KTGF model in dense flows such as adding an effective restitution coefficient, coupling the KTGF model with local rheological models (such as the $\mu(I)$ law), adding a new rotational viscosity computed from the rotational granular temperature or taking into account friction from microscopic structures

formation. More information can be found in [61]. Khalilitehrani et al. [46] used the two models with switching conditions: the dense granular flow model for dense granular flows (solid volume fraction higher than 0.52) and the KTGF model for dilute granular flows (lower than 0.52).

On the other hand, for high rotation speed, the granular temperature is higher due to larger velocity fluctuations, increasing the granular shear viscosity. This explains why the KTGF model best captures the dense granular flow in a rotating drum for high rotation speed [24,25]. Yet, even at high rotation speed, a small deviation appears between the experiment and the simulation in the middle of the rotating drum.

The “liquid” regime, where solid inertia becomes important but particles are always in contact with each other [2], is better represented by the dense granular flow model [34] for which the model was developed for. The “liquid” regime is typically the type of solid flow inside a rotating drum. This means that the dense granular flow model is more adapted to capture the solid rheology in a rotating drum compared to the KTGF model.

Moreover, the model used for dense granular flow is numerically less complex and easier to implement than the KTGF model. Indeed, the granular flow model is 2.3 times faster than KTGF model, for the same number of processors used. Indeed, multiphase solver requires more computational resources and can lead to computational divergence in some cases. The VOF approach is more stable with the dense granular flow model.

With all the information mentioned, it was quite obvious that the $\mu(I)$ model based on Mohr-coulomb law is more suitable for dense granular flow dominated by multiple particle interaction compared to the KTGF which is more adapted for homogeneous gas-solid flows. Yet, recent studies used the KTGF model for modelling dense solid flow inside a rotating drum [24–27,62]. Moreover, some authors also used the KTGF model for dense granular flow in different apparatus [63–65]. The dense granular flow model should be used for such flow regime. Moreover, this study shows that the $\mu(I)$ law is easier to calibrate, as most of the parameters are based on experimental data obtained from the rotating drum, and quicker to compute compared to the KTGF model.

The aim of this work was therefore to illustrate that $\mu(I)$-type models are indeed better suited to dense flow in a rotating drum at low rotational speed (*i.e.* for surging, rolling and cascading regimes inside a rotating drum). In some cases, the cited articles that used the KTGF model for modelling powder flow in a rotating drum were for a Froude number lower than 10^{-1}. For such Froude number or higher the KTGF may be more appropriate as the flow type for such Froude numbers corresponds to cataracting, which is closer to a gas-solid flow regime.

5. CONCLUSION

In this study, two CFD models for dense powder flow in a rotating drum are compared and confronted to experimental results. The rotating drum (GranuDrum™) operates between 1 and 10 RPM and three powders with different flowabilities were studied. The two CFD models are the Kinetic Theory of Granular Flow (KTGF) and the dense granular flow model, also called the $\mu(I)$ law.

The GranuDrum™ software measures powder flowability properties based on the interface of the powder for a given rotation speed. The selected parameters were the dynamic angle of repose and the cohesive index. Both parameters are important to assess the powder flowability. As the software does not provide the interface coordinate, an image processing code was developed (written in Python) to extract these coordinates. Having the interface coordinates is crucial when comparing the CFD with the experiment.

For any powder, the KTGF model fails to capture the powder rheology for low rotation speed (lower or equal to 2 RPM). Yet, for higher rotation speed (higher or equal to 4 RPM), the model gets closer to the averaged experimental interface. This is in agreement with the assumption on the model: the KTGF model is more adapted for the “gaseous” regime. Indeed, the solid viscosity depends on the granular temperature. The latter is negligible for low rotation speed as it depends on the solid velocity fluctuation. When the rotation speed increases, the powder is more agitated, meaning that the granular temperature acts more significantly on the solid viscosity.

Regarding the dense granular model, the model is relatively close to the experiment, for any studied rotation speed and powder. This model is more adapted for the “liquid” regime, which is exactly the type of flow in a rotating drum for Froude number lower than 10^{-1}. However, the model has more difficulty to catch the powder rheology for poor flowable powder, especially with rice flour. The rheology for cohesive powders is still a work in progress in the literature.

The parameters for the dense granular model are directly taken from experimental data obtained from the rotating drum. The KTGF model parameters are much more complex to measure and each viscosity contribution can be computed with different models. The KTGF model is much more complex to parameterise. Moreover, the dense granular model is computed with a Volume of Fluid (VoF) approach, which requires less computational resources compared to the KTGF model, which is computed with a multiphase Euler-Euler solver.

Once that the rheological CFD model is calibrated, it could be used to study the solid flow inside gas/solid contactors. In this work, we recommend using the dense granular flow model for dense granular flow systems while using the KTGF model for gas-solid flow systems. Future work will be conducted on the former.

REFERENCES

[1] J.C. Charpentier, T.F. McKenna, Managing complex systems: some trends for the future of chemical and process engineering, Chem. Eng. Sci. 59 (2004) 1617–1640. https://doi.org/10.1016/j.ces.2004.01.044.

[2] G.D.R. Midi, On dense granular flows, Eur. Phys. J. E. 14 (2004) 341–365. https://doi.org/10.1140/epje/i2003-10153-0.

[3] Y. Forterre, O. Pouliquen, Flows of dense granular media, Annu. Rev. Fluid Mech. 40 (2008) 1–24. https://doi.org/10.1146/annurev.fluid.40.111406.102142.

[4] M. Leturia, M. Benali, S. Lagarde, I. Ronga, K. Saleh, Characterization of flow properties of cohesive powders: A comparative study of traditional and new testing methods, Powder Technol. 253 (2014) 406–423. https://doi.org/10.1016/j.powtec.2013.11.045.

[5] A. Saker, M.G. Cares-Pacheco, P. Marchal, V. Falk, Powders flowability assessment in granular compaction: What about the consistency of Hausner ratio?, Powder Technol. 354 (2019) 52–63. https://doi.org/10.1016/j.powtec.2019.05.032.

[6] H.M. Beakawi Al-Hashemi, O.S. Baghabra Al-Amoudi, A review on the angle of repose of granular materials, Powder Technol. 330 (2018) 397–417. https://doi.org/10.1016/j.powtec.2018.02.003.

[7] J. Mellmann, The transverse motion of solids in rotating cylinders-forms of motion and transition behavior, Powder Technol. 118 (2001) 251–270. https://doi.org/10.1016/S0032-5910(00)00402-2.

[8] G. Lumay, A. Neveu, F. Francqui, Measuring Powder Flow Properties in a Rotating Drum, SSRN Electron. J. 200 (2022) 111548. https://doi.org/10.2139/ssrn.4040037.

[9] A.S. Bongo Njeng, S. Vitu, M. Clausse, J.L. Dirion, M. Debacq, Effect of lifter shape and operating parameters on the flow of materials in a pilot rotary kiln: Part I. Experimental RTD and axial dispersion study, Powder Technol. 269 (2015) 554–565. https://doi.org/10.1016/j.powtec.2014.03.066.

[10] L. Chatre, M. Bataille, M. Debacq, T. Randriamanantena, J. Nos, F. Herbelet, Modelling of powder hydrodynamics in a screw reactor, Powder Technol. 420 (2023) 118367. https://doi.org/10.1016/j.powtec.2023.118367.

[11] K. Malhotra, A.S. Mujumdar, M. Miyahara, Estimation of particle renewal rates along the wall in a mechanically stirred granular bed, Chem. Eng. Process. 27 (1990) 121–130. https://doi.org/10.1016/0255-2701(90)87001-Y.

[12] B. Daumann, A. Fath, H. Anlauf, H. Nirschl, Determination of the mixing time in a discontinuous powder mixer by using image analysis, Chem. Eng. Sci. 64 (2009) 2320–2331. https://doi.org/10.1016/j.ces.2009.01.032.

[13] J.M.N.T. Gray, Granular flow in partially filled slowly rotating drums, J. Fluid Mech. 441 (2001) 1–29. https://doi.org/10.1017/S0022112001004736.

[14] O. Dubé, E. Alizadeh, J. Chaouki, F. Bertrand, Dynamics of non-spherical particles in a rotating drum, Chem. Eng. Sci. 101 (2013) 486–502. https://doi.org/10.1016/j.ces.2013.07.011.

[15] X. Liu, C. Zhang, J. Zhan, Quantitative comparison of image analysis methods for particle mixing in rotary drums, Powder Technol. 282 (2015) 32–36. https://doi.org/10.1016/j.powtec.2014.08.076.

[16] P.W. Cleary, Large scale industrial DEM modelling, Eng. Comput. (Swansea, Wales). 21 (2004) 169–204. https://doi.org/10.1108/02644400410519730.

[17] H. Fan, D. Guo, J. Dong, X. Cui, M. Zhang, Z. Zhang, Discrete element method simulation of the mixing process of particles with and without cohesive interparticle forces in a fluidized bed, Powder Technol. 327 (2018) 223–231. https://doi.org/10.1016/j.powtec.2017.12.016.

[18] F. Tian, M. Zhang, H. Fan, M. Gu, L. Wang, Y. Qi, Numerical study on microscopic mixing characteristics in fluidized beds via DEM, Fuel Process. Technol. 88 (2007) 187–198. https://doi.org/10.1016/j.fuproc.2006.04.006.

[19] N. Govender, A DEM study on the thermal conduction of granular material in a rotating drum using polyhedral particles on GPUs, Chem. Eng. Sci. 252 (2022) 117491.

https://doi.org/10.1016/j.ces.2022.117491.
[20] Y. Xu, C. Xu, Z. Zhou, J. Du, D. Hu, 2D DEM simulation of particle mixing in rotating drum: A parametric study, Particuology. 8 (2010) 141–149. https://doi.org/10.1016/j.partic.2009.10.003.
[21] P.Y. Liu, R.Y. Yang, A.B. Yu, DEM study of the transverse mixing of wet particles in rotating drums, Chem. Eng. Sci. 86 (2013) 99–107. https://doi.org/10.1016/j.ces.2012.06.015.
[22] N. Gui, J. Yan, W. Xu, L. Ge, D. Wu, Z. Ji, J. Gao, S. Jiang, X. Yang, DEM simulation and analysis of particle mixing and heat conduction in a rotating drum, Chem. Eng. Sci. 97 (2013) 225–234. https://doi.org/10.1016/j.ces.2013.04.005.
[23] C.A. Radeke, B.J. Glasser, J.G. Khinast, Large-scale powder mixer simulations using massively parallel GPUarchitectures, Chem. Eng. Sci. 65 (2010) 6435–6442. https://doi.org/10.1016/j.ces.2010.09.035.
[24] D.A. Santos, I.J. Petri, C.R. Duarte, M.A.S. Barrozo, Experimental and CFD study of the hydrodynamic behavior in a rotating drum, Powder Technol. 250 (2013) 52–62. https://doi.org/10.1016/j.powtec.2013.10.003.
[25] W. Rong, Y. Feng, P. Schwarz, P. Witt, B. Li, T. Song, J. Zhou, Numerical study of the solid flow behavior in a rotating drum based on a multiphase CFD model accounting for solid frictional viscosity and wall friction, Powder Technol. 361 (2020) 87–98. https://doi.org/10.1016/j.powtec.2019.10.034.
[26] A.N. Huang, H.P. Kuo, CFD simulation of particle segregation in a rotating drum. Part I: Eulerian solid phase kinetic viscosity, Adv. Powder Technol. 28 (2017) 2094–2101. https://doi.org/10.1016/j.apt.2017.05.016.
[27] M.A. Delele, F. Weigler, G. Franke, J. Mellmann, Studying the solids and fluid flow behavior in rotary drums based on a multiphase CFD model, Powder Technol. 292 (2016) 260–271. https://doi.org/10.1016/j.powtec.2016.01.026.
[28] A.M.G. Arseni, G. De Monaco, F. Greco, P.L. Maffettone, Granular flow in rotating drums through simulations adopting a continuum constitutive equation, Phys. Fluids. 32 (2020). https://doi.org/10.1063/5.0018694.
[29] C.K.K. Lun, S.B. Savage, D.J. Jeffrey, N. Chepurniy, Kinetic theories for granular flow: Inelastic particles in Couette flow and slightly inelastic particles in a general flowfield, J. Fluid Mech. 140 (1984) 223–256. https://doi.org/10.1017/S0022112084000586.
[30] B.G.M. Van Wachem, J.C. Schouten, C.M. Van den Bleek, R. Krishna, J.L. Sinclair, Comparative analysis of CFD models of dense gas-solid systems, AIChE J. 47 (2001) 1035–1051. https://doi.org/10.1002/aic.690470510.
[31] D.J. Patil, J. Smit, M. Van Sint Annaland, J.A.M. Kuipers, Wall-to-bed heat transfer in gas-solid bubbling fluidized beds, AIChE J. 52 (2006) 58–74. https://doi.org/10.1002/aic.10590.
[32] L. Yu, J. Lu, X. Zhang, S. Zhang, Numerical simulation of the bubbling fluidized bed coal gasification by the kinetic theory of granular flow (KTGF), Fuel. 86 (2007) 722–734. https://doi.org/10.1016/j.fuel.2006.09.008.
[33] C.G. Philippsen, A.C.F. Vilela, L.D. Zen, Fluidized bed modeling applied to the analysis of processes: Review and state of the art, J. Mater. Res. Technol. 4 (2015) 208–216. https://doi.org/10.1016/j.jmrt.2014.10.018.
[34] P. Jop, Y. Forterre, O. Pouliquen, A constitutive law for dense granular flows, Nature. 441 (2006) 727–730. https://doi.org/10.1038/nature04801.
[35] L. Bennani, H. Neau, C. Baudry, J. Laviéville, P. Fede, O. Simonin, Numerical simulation of unsteady dense granular flows with rotating geometries, Chem. Eng. Res. Des. 120 (2017) 333–347. https://doi.org/10.1016/j.cherd.2017.01.028.
[36] J. Chauchat, Z. Cheng, T. Nagel, C. Bonamy, T.J. Hsu, SedFoam-2.0: A 3-D two-phase flow numerical model for sediment transport, Geosci. Model Dev. 10 (2017) 4367–4392. https://doi.org/10.5194/gmd-10-4367-2017.
[37] L. Staron, P.Y. Lagrée, S. Popinet, Continuum simulation of the discharge of the granular silo:A validation test for the μ(I) visco-Plastic flow law, Eur. Phys. J. E. 37 (2014). https://doi.org/10.1140/epje/i2014-14005-6.

[38] P.B. Kowalczuk, J. Drzymala, Physical meaning of the Sauter mean diameter of spherical particulate matter, Part. Sci. Technol. 34 (2016) 645–647. https://doi.org/10.1080/02726351.2015.1099582.
[39] D. Geldart, Types of gas fluidization, Powder Technol. 7 (1973) 285–292. https://doi.org/10.1016/0032-5910(73)80037-3.
[40] L. Chatre, J. Socci, S.J. Adams, P. Denissenko, N. Cherkasov, Design of 3D-printed structures for improved mass transfer and pressure drop in packed-bed reactors, Chem. Eng. J. 420 (2021) 129762. https://doi.org/10.1016/j.cej.2021.129762.
[41] D.J. Bora, A.K. Gupta, F.A. Khan, Comparing the Performance of L*A*B* and HSV Color Spaces with Respect to Color Image Segmentation, (2015). http://arxiv.org/abs/1506.01472.
[42] T. Chai, R.R. Draxler, Root mean square error (RMSE) or mean absolute error (MAE)? -Arguments against avoiding RMSE in the literature, Geosci. Model Dev. 7 (2014) 1247–1250. https://doi.org/10.5194/gmd-7-1247-2014.
[43] C.J. Willmott, K. Matsuura, Advantages of the mean absolute error (MAE) over the root mean square error (RMSE) in assessing average model performance, Clim. Res. 30 (2005) 79–82. https://doi.org/10.3354/cr030079.
[44] K.G. Bilde, J. Hærvig, Aggregation and breakage of solid particles in a turbulent flow through a 90◦ pipe bend using CFD-PBE, in: 2022: pp. 9–11.
[45] J.T. Jenkins, Dense shearing flows of inelastic disks, Phys. Fluids. 18 (2006). https://doi.org/10.1063/1.2364168.
[46] M. Khalilitehrani, P.J. Abrahamsson, A. Rasmuson, Modeling dilute and dense granular flows in a high shear granulator, Powder Technol. 263 (2014) 45–49. https://doi.org/10.1016/j.powtec.2014.04.088.
[47] H. Derijani, L.A. James, R.D. Haynes, Evaluation of the interFoam solver in the prediction of immiscible two-phase flow in imbibition and drainage on the pore-doublet system, E3S Web Conf. 366 (2023) 1–8. https://doi.org/10.1051/e3sconf/202336601017.
[48] P. Jop, Ecoulements granulaires sur fond meuble, PhD Thesis, Université de Provence, 2006.
[49] N. Berger, E. Azéma, J.F. Douce, F. Radjai, Scaling behaviour of cohesive granular flows, Epl. 112 (2015). https://doi.org/10.1209/0295-5075/112/64004.
[50] Q. Laine, T. Randriamanantena, F. Lamadie, E. Olmos, Experimental study of velocity and turbulence fields in a square mixer-settler tank: Comparison of shake the box PTV and 2D2C PIV, Chem. Eng. Sci. 275 (2023) 118636. https://doi.org/10.1016/j.ces.2023.118636.
[51] R. Zadghaffari, J.S. Moghaddas, J. Revstedt, A mixing study in a double-Rushton stirred tank, Comput. Chem. Eng. 33 (2009) 1240–1246. https://doi.org/10.1016/j.compchemeng.2009.01.017.
[52] L. Chatre, M. Bataille, M. Debacq, K. Lachin, T. Randriamanantena, J. Nos, F. Herbelet, Study of local powder mixing in a screw reactor: Characterisation of the active layer renewal, Powder Technol. 439 (2024) 119729. https://doi.org/10.1016/j.powtec.2024.119729.
[53] U. Vengateson, R. Mohan, Experimental and modeling study of fluidized bed granulation: Effect of binder flow rate and fluidizing air velocity, Resour. Technol. 2 (2016) S124–S135. https://doi.org/10.1016/j.reffit.2016.10.003.
[54] M. Askarishahi, M.S. Salehi, S. Radl, Capability of the TFM Approach to Predict Fluidization of Cohesive Powders, Ind. Eng. Chem. Res. 61 (2022) 3186–3205. https://doi.org/10.1021/acs.iecr.1c04786.
[55] C. Gallagher, S. Jalalifar, F. Salehi, A. Kourmatzis, S. Cheng, A two-fluid model for powder fluidisation in turbulent channel flows, Powder Technol. 389 (2021) 163–177. https://doi.org/10.1016/j.powtec.2021.05.019.
[56] M. Macaulay, P. Rognon, Viscosity of cohesive granular flows, Soft Matter. 17 (2021) 165–173. https://doi.org/10.1039/d0sm01456g.
[57] A. Gans, A. Abramian, P.Y. Lagrée, M. Gong, A. Sauret, O. Pouliquen, M. Nicolas,

Collapse of a cohesive granular column, J. Fluid Mech. 959 (2023) 1–17. https://doi.org/10.1017/jfm.2023.180.
[58] S. Mandal, M. Nicolas, O. Pouliquen, Insights into the rheology of cohesive granular media, Proc. Natl. Acad. Sci. U. S. A. 117 (2020) 8366–8373. https://doi.org/10.1073/pnas.1921778117.
[59] M. He, B. Zhao, J. Xu, L. Kong, J. Wang, Assessment of kinetic theory for gas–solid flows using discrete particle method, Phys. Fluids. 34 (2022). https://doi.org/10.1063/5.0117386.
[60] J. Dou, L. Wang, W. Ge, J. Ouyang, Effect of mesoscale structures on solid phase stress in gas–solid flows, Chem. Eng. J. 455 (2023) 140825. https://doi.org/10.1016/j.cej.2022.140825.
[61] K. Wu, V. Francia, M.O. Coppens, Dynamic viscoplastic granular flows: A persistent challenge in gas-solid fluidization, Powder Technol. 365 (2020) 172–185. https://doi.org/10.1016/j.powtec.2019.04.053.
[62] W. Mendonça Benedito, C.R. Duarte, M.A. de Souza Barrozo, D. Araújo dos Santos, An investigation of CFD simulations capability in treating non-spherical particle dynamics in a rotary drum, Powder Technol. 332 (2018) 171–177. https://doi.org/10.1016/j.powtec.2018.03.067.
[63] X. Shi, F. Ronsse, J. Roegiers, J.G. Pieters, 3D Eulerian-Eulerian modeling of a screw reactor for biomass tachermochemical conversion. Part 1: Solids flow dynamics and back-mixing, Renew. Energy. 143 (2019) 1465–1476. https://doi.org/10.1016/j.renene.2019.05.098.
[64] A. Darelius, A. Rasmuson, B. van Wachem, I. Niklasson Björn, S. Folestad, CFD simulation of the high shear mixing process using kinetic theory of granular flow and frictional stress models, Chem. Eng. Sci. 63 (2008) 2188–2197. https://doi.org/10.1016/j.ces.2008.01.018.
[65] B.H. Ng, Y.L. Ding, M. Ghadiri, Modelling of dense and complex granular flow in high shear mixer granulator-A CFD approach, Chem. Eng. Sci. 64 (2009) 3622–3632. https://doi.org/10.1016/j.ces.2009.05.011.